Theoretical analysis of mixing in liquid clouds. Part IV: DSD evolution

and mixing diagrams

Mark Pinsky, and Alexander Khain

Department of Atmospheric Sciences, The Hebrew University of Jerusalem, Israel

Submitted to

Atmospheric Chemistry and Physics

May 2017

Revised September 2017

Communicating author: Alexander Khain, The Hebrew University of Jerusalem, khain@vms.huji.ac.il

27   **Abstract**

28   Evolution of droplet size distribution (DSD) due to mixing between cloudy and dry

29   volumes is investigated for different values of the cloud fraction and different initial DSD

30   shapes. The analysis is performed using a diffusion-evaporation model which describes time-

31   dependent processes of turbulent diffusion and droplet evaporation within a mixing volume.

32   Time evolution of the DSD characteristics such as droplet concentration, LWC, mean volume

33   and the effective radii is analyzed. The mixing diagrams are plotted for the final mixing

34   stages. It is shown that the difference between the mixing diagrams for homogeneous and

35   inhomogeneous mixing is insignificant and decreases with an increase in the DSD width. The

36   dependencies of normalized cube of the effective radius on the cloud fraction were compared

37   with those on normalized droplet concentration and found to be quite different. In case the

38   normalized droplet concentration is used, mixing diagrams do not show any significant

39   dependence on relative humidity in the dry volume.

40   The main conclusion of the study is that traditional mixing diagrams cannot serve as a

41   reliable tool for analysis of mixing type.

43   **Keywords:** turbulent mixing, droplet evaporation, DSD evolution, mixing diagram

1. Introduction

The effects of mixing of cloudy air with surrounding dry air on cloud microphysics are still the focus of many studies (see overview by Devenish et al., 2012). Processes of mixing are investigated in observations (Yum et al., 2015; Bera at al., 2016a,b), Large Eddy Simulations (Andrejczuk et al., 2009; Khain et al., 2017), Direct Numerical Simulations (Kumar et al., 2014, 2017). Processes of mixing and their effects on droplet size distributions were recently investigated in a set of theoretical studies (Yang et al., 2016; Korolev et al., 2016 (hereafter, Pt1); Pinsky et al., 2016 a,b). The Pt1 presented analysis of conventional (classical) concept of mixing and introduced the main parameters characterizing homogeneous and extremely inhomogeneous mixing. At a monodisperse initial droplet size distribution (DSD), homogeneous mixing leads to a decrease in droplet size and droplet mass content, while the number of droplets remains unchanged. Extremely inhomogeneous mixing is characterized by decreasing the number of droplets due to full evaporation of some fraction of droplets penetrating the initially dry air volume while the DSD shape in the cloud volume remains unchanged. As a result of extremely inhomogeneous mixing, droplet concentration decreases while the mean volume radii remain unchanged. At a polydisperse DSDs, the extreme homogeneous mixing is characterized by proportional changes in DSD for all droplet radii (Pt1). Since widely used mixing diagrams describe the final equilibrium stage of mixing they do not contain information about changes in microphysical quantities in the course of mixing.

Pinsky et al. (2016a, hereafter Pt2) analyzed the time evolution of monodisperse and polydisperse DSD during homogeneous mixing. It was shown that result of mixing strongly depends on the shape of the initial DSD. At a wide DSD, evaporation of droplets (first of all, of the smallest ones) is not accompanied by a decrease in the effective radius. Moreover, this radius may even increase over time. This result indicates that the widely used criterion of separation of mixing types based on the behavior of the effective radius during mixing is not generally relevant and may be wrong in application to real clouds.

71   Pinsky et.al. (2016b, hereafter Pt3) introduced a diffusion-evaporation model which

72   describes evolution DSDs and all the microphysical variables due to two simultaneously

73   occurring processes: turbulent diffusion and droplet evaporation. Mixing between two equal

74   volumes of subsaturated and cloudy air was analyzed, i.e. it was assumed that the cloud

75   volume fraction $\mu = 1/2$. The initial DSD in the cloudy volume was assumed monodisperse.

76   These simplified assumptions allowed to reduce the turbulent mixing equations to two-

77   parametric ones. The first parameter is the Damkölher number, Da, which is the ratio of the

78   characteristic mixing time to the characteristic phase relaxation time. The second parameter is

79   the potential evaporation parameter R characterizing the ratio between the amount of water

80   vapor needed to saturate the initially dry volume and the amount of available liquid water in

81   the cloudy volume.

82   Within the $Da - R$ space, in addition to the two extreme mixing types defined in the

83   classical concept, two more mixing regimes were distinguished, namely, intermediate and

84   inhomogeneous mixing. It was shown that any type of mixing leads to formation of a tail of

85   small droplets, i.e. to DSD broadening. It was also shown that the relative humidity in the

86   initially dry volume rapidly increases due to both water vapor diffusion and evaporation of

87   penetrating droplets. As a result, the effective radii in the initially dry volume rapidly

88   approach the values typical of cloudy volume. At the same time, the liquid water content

89   (LWC) remains significantly lower than that in the cloudy volume during much longer time

90   than required for the effective droplet radius to grow.

91   In the present study (Pt4) we continue investigating the turbulent mixing between an

92   initially dry volume and a cloudy volume. The focus of the study is investigation of DSD

93   temporal evolution and analysis of the final equilibrium DSD. In comparison to Pt3, the

94   problem analyzed in this study is more sophisticated in several aspects:

95   • The dependences of different mixing characteristics on cloud volume fraction $0 \le \mu \le 1$

96   are analyzed. In this case the equations of turbulent mixing cannot be reduced to the two-

97   parametric problem as it was done in Pt3.

98   • The initial DSDs in cloud volume are polydisperse. We use both narrow and wide

99   initial DSD described by Gamma distributions with different sets of parameters. The DSD are

100   the same as those used in Pt2. Mechanisms of formation of wide DSDs in clouds including

101   DSDs in undiluted cloud cores were investigated in several studies [e.g., Khain et al., 2000;

102   Pinky and Khain, 2002; Segal et al., 2004; Prabha et al., 2011]. These studies show the DSD

103   broadening is caused by in-cloud nucleation of droplets within clouds as well as by collisions.

104   It was shown that DSDs in adiabatic volumes can be wide and first raindrops or drizzle drop

105   arise namely in non-diluted adiabatic cloud parcels [Khain et al., 2013; Magaritz-Ronen et al.,

106   2016]. We use both narrow and wide DSDs in the form of Gamma distribution with typical

107   parameters used in different cloud resolving models. The DSDs that are used as initial ones in

108   cloudy volumes could be formed also under influence of mixing during their previous history.

109   It does not affect our analysis.

110   • The equation for supersaturation, used in this study, is valid at low humidity in the

111   initially dry volume and is more general and compared with that used in Pt3, which makes the

112   DSD calculations more accurate.

113   At the same time, some simplifications used in Pt3 are retained in this study. The vertical

114   movement of the entire mixing volume is neglected; collisions between droplets and droplet

115   sedimentation are not allowed. Also, we consider a 1D diffusion-evaporation problem. We

116   neglect the changes of temperature in the course of mixing, which is possibly a less significant

117   simplification. All these simplifications allow to reveal the effects of turbulent mixing and

118   evaporation on DSD evolution.

119

120   **2. Formulation of the problem and model design**

121   In this study, the process of mixing is investigated basing on the solution of 1D diffusion-

122   evaporation equation (see also Pt3). According to this equation, evaporation of droplets due to

123   negative supersaturation in the mixing volume takes place simultaneously with turbulent

124   mixing. Since droplets within the volume are under different negative supersaturation values

125   until the final equilibrium is reached, the modeled mixing is inhomogeneous. The droplets can

126   evaporate either partially or totally. The evaporation leads to a decrease in droplet sizes and in

127   droplet concentration.

128   Like in Pt3, the process of turbulent diffusion is described by a 1D equation of turbulent

129   diffusion. The equation does not describe formation of separate turbulent filaments. Instead, it

130   describes averaged effects of turbulent mixing by modeling of turbulent diffusion, characterized

131   by a typical value of turbulent diffusion coefficient K. The mixing is assumed to be driven by

132   isotropic turbulence at scales within the inertial sub-range where Richardson's law is valid. In

133   this case, turbulent coefficient is evaluated as in Monin and Yaglom (1975).

134    $K(L) = C\varepsilon^{1/3}L^{4/3}$ (1)

135   In Eq. (1) ε is the turbulent kinetic energy dissipation rate and $C = 0.2$ is a constant (Monin

136   and Yaglom, 1975), Boffetta and Sokolov (2002). Eq. (1) means that we consider the effects

137   of turbulent diffusion at scales much larger than the Kolmogorov microscale, i.e. the effects of

138   molecular diffusion are neglected. In the simulations, we use $L = 40$ m and $\varepsilon = 20\,cm^2 s^{-3}$.

139

140   ***Geometry of mixing and the initial conditions***

141   The conceptual scheme presenting mixing geometry and the initial conditions used in the

142   following analysis are shown in **Figure 1**.

143

144   **Fig 1 here**

145

146   At $t = 0$ the mixing volume of length L is divided into two volumes: the cloud volume of

147   length μL (Fig.1, left) and the dry volume of length $(1-\mu)L$ (Fig.1, right), where $0 \leq \mu \leq 1$

148   is the cloud volume fraction. The entire volume is assumed closed, i.e. adiabatic. At $t = 0$ the

149   cloud volume is assumed saturated, so the supersaturation $S_1 = 0$. This volume is also

150   characterized by the initial distribution of the square of the droplet radii $g_1(\sigma)$, where $\sigma = r^2$.

151   The initial liquid water mixing ratio in the cloudy volume is equal to

152    $q_{w1} = \dfrac{4\pi\rho_w}{3\rho_a} \displaystyle\int_0^\infty \sigma^{3/2} g_1(\sigma) d\sigma$. The integral of $g_1(\sigma)$ over σ is equal to the initial droplet

153   concentration in the cloud volume $N_1 = \displaystyle\int_0^\infty g_1(\sigma) d\sigma$. The initial droplet concentration in the

154   dry volume is $N_2 = 0$, the initial negative supersaturation in this volume is $S_2 < 0$ and the

155   initial liquid water mixing ratio $q_{w2} = 0$. Therefore, the initial profiles of these quantities

156   along the x-axis are step functions:

157

158    $N(x,0) = \begin{cases} N_1 & \text{if} & 0 \leq x < \mu L \\ 0 & \text{if} & \mu L \leq x < L \end{cases}$ (2a)

159    $S(x,0) = \begin{cases} 0 & \text{if} & 0 \leq x < \mu L \\ S_2 & \text{if} & \mu L \leq x < L \end{cases}$ (2b)

160    $q_w(x,0) = \begin{cases} q_{w1} & \text{if} & 0 \leq x < \mu L \\ 0 & \text{if} & \mu L \leq x < L \end{cases}$ (2c)

161

162   The initial profile of droplet concentration is shown in Fig. 1b. This is the simplest

163   inhomogeneous mixing scheme, wherein mixing takes place only in the x-direction, and the

164   vertical velocity is neglected.

165   Since the total volume is adiabatic, the fluxes of different quantities through the left and

166   right boundaries at any time instance are equal to zero, i.e.

167

168   $\dfrac{\partial N(0,t)}{\partial x} = \dfrac{\partial N(L,t)}{\partial x} = 0$; $\dfrac{\partial q_w(0,t)}{\partial x} = \dfrac{\partial q_w(L,t)}{\partial x} = 0$; $\dfrac{\partial q_v(0,t)}{\partial x} = \dfrac{\partial q_v(L,t)}{\partial x} = 0$ (3)

169   where q_v is the water vapor mixing ratio.

170   To investigate of mixing process for different initial DSD, we assume that DSD in the cloud

171   volume can be represented by a Gamma distribution:

172   $f(r,t=0) = \dfrac{N_0}{\Gamma(\alpha)\beta}\left(\dfrac{r}{\beta}\right)^{\alpha-1} \exp\left(-\dfrac{r}{\beta}\right)$ (4)

173   where N_0 is an intercept parameter, α is a shape parameter and β is a slope parameter of

174   distribution. The DSD $f(r)$ relates to distribution $g_1(\sigma)$ as $f(r) = 2rg_1(\sigma)$. We performed

175   simulations with both initially wide and narrow DSDs. The width of DSD is determined by a

176   set of parameters. The parameters of the initial Gamma distributions used in this study are

177   presented in **Table 1**. Parameters of the distributions are chosen in such a way that the modal

178   radii of DSD and the values of LWC are the same for both distributions. These distributions

179   were used in Pt2 for analysis of homogeneous mixing.

180

181   **Table 1 here**

182

183

184   *Conservative quantity* $\Gamma(x,t)$

185   The supersaturation equation for an adiabatic immovable volume can be written in the

186   form $\dfrac{1}{S+1}\dfrac{dS}{dt} = -A_2\dfrac{dq_w}{dt}$, where S is supersaturation over water, and the coefficient

187   $A_2 = \dfrac{1}{q_v} + \dfrac{L_w^2}{c_p R_v T^2}$ is slightly dependent on temperature (Korolev and Mazin, 2003) (notations

188   of other variables are presented in **Appendix**). In our analysis we consider A_2 to be a

189   constant. As follows from the supersaturation equation, the quantity

190

191    $\Gamma(x,t) = \ln\left[S(x,t)+1\right] + A_2 q_w(x,t)$ (5)

192

193   is a conservative quantity, i.e. it is invariant with respect to phase transitions. In Eq. (5),

194    $\left|S(x,t)\right|$ can be comparable with unity by the order of magnitude. The conservative quantity

195    $\Gamma(x,t)$ obeys the following equation for turbulent diffusion

196

197    $\dfrac{\partial \Gamma(x,t)}{\partial t} = K\dfrac{\partial^2 \Gamma(x,t)}{\partial x^2}$ (6)

198

199   with the adiabatic (no flux) condition at the left and right boundaries $\dfrac{\partial \Gamma(0,t)}{\partial x} = \dfrac{\partial \Gamma(L,t)}{\partial x} = 0$

200   and the initial profile at $t=0$

201

202    $\Gamma(x,0) = \begin{cases} A_2 q_{w1} & \text{if} & 0 \le x < \mu L \\ \ln\left[S_2 + 1\right] & \text{if} & \mu L \le x < L \end{cases}$ (7)

203

204   From Eq. (7) it follows that $\Gamma(x,0)$ is positive in the cloud volume and negative in the

205   initially dry volume. The mean value of function $\Gamma(x,0)$ can be written as follows:

206

207    $\bar{\Gamma} = \dfrac{1}{L}\int\limits_0^L \Gamma(x,0)dx = \dfrac{A_2 q_{w1}}{L}\int\limits_0^{\mu L} dx + \dfrac{\ln\left[S_2+1\right]}{L}\int\limits_{\mu L}^L dx = \mu A_2 q_{w1} + (1-\mu)\ln\left[S_2+1\right]$ (8)

208

209    $\bar{\Gamma}$ can be either positive or negative. In the latter case a complete evaporation of droplets in the

210   course of mixing takes place.

211   The solution of Eq. (6) with the initial condition (7) is (Polyanin et al., 2004):

$$\Gamma(x,t) = \sum_{n=0}^{\infty} a_n \exp\left(-\frac{Kn^2\pi^2 t}{L^2}\right)\cos\left(\frac{n\pi x}{L}\right) =$$

212 $\mu A_2 q_{w1} + (1-\mu)\ln\left[S_2 + 1\right] -$ (9)

$$2\left(\ln\left[S_2 + 1\right] - A_2 q_{w1}\right)\sum_{n=1}^{\infty}\frac{\sin(n\pi\mu)}{n\pi}\exp\left(-\frac{Kn^2\pi^2 t}{L^2}\right)\cos\left(\frac{n\pi x}{L}\right)$$

213 One can see that function $\Gamma(x,t)$ depends on three independent parameters $A_2 q_{w1}$, S_2 and μ.

214 This function does not depend on the shape of the initial DSD in the cloud volume. In the final

215 state when $t \to \infty$, $\Gamma(x,t)$ is :

216 $\Gamma(t=\infty) = \mu A_2 q_{w1} + (1-\mu)\ln\left[S_2 + 1\right]$ (10)

217 Therefore, $\Gamma(t=\infty)$ depends on the cloud fraction and the initial values of liquid water

218 mixing ratio in the cloud volume and the relative humidity in initially dry volume.

219 The final equilibrium values of supersaturation $S(x,\infty)$ and liquid water mixing ratio

220 $q_w(x,\infty)$ can be calculated using Eq. (5). The case $\Gamma(t=\infty) > 0$ corresponds to the

221 equilibrium state with $S(x,\infty) = 0$ and $q_w(x,\infty) = \mu q_{w1} + (1-\mu)\dfrac{\ln\left[S_2 + 1\right]}{A_2}$. The case

222 $\Gamma(t=\infty) < 0$ corresponds to the equilibrium state with $q_w(x,\infty) = 0$ and

223 $S(x,\infty) = (1+S_2)^{1-\mu}\exp\left(\mu A_2 q_{w1}\right) - 1$. At given q_{w1} and S_2, there is a critical value of the

224 cloud fraction μ_{cr} which separates these two possible final equilibrium states. This critical

225 value corresponds to $\Gamma(t=\infty) = 0$ and can be calculated from Eq. (10) as:

226

227 $\mu_{cr} = \dfrac{\ln\left[S_2 + 1\right]}{\ln\left[S_2 + 1\right] - A_2 q_{w1}}$ (11)

228

229 Another expression for μ_{cr} was formulated in Pt1.

230 The examples of spatial-temporal variations of function $\Gamma(x,t)$ for different cloud

231 fractions and initial RH=80% are shown in **Figure 2.**

232

233   **Fig 2 here**

234

235   Upper panels $\mu = 0.1$ correspond to the case of final total droplet evaporation and negative

236   final function Γ, whereas the middle and bottom rows $\mu = 0.5$ and $\mu = 0.9$ illustrate partial

237   evaporation cases when the total mixing volume reaches saturation. It is interesting that the

238   time required for the final equilibrium state to be reached practically does not depend on the

239   cloud fraction, being ~180 seconds for the illustrated cases. The cases $\mu = 0.1$ and $\mu = 0.9$

240   demonstrate a strong non-symmetric spatial variability of $\Gamma(x)$ function during the first 50

241   seconds.   At $\mu = 0.5$, a nearly full compensation between saturation deficit in the dry

242   volume and available liquid water in the cloud volume takes place if at the equilibrium state

243     $S(x,\infty) = q_w(x,\infty) = \Gamma(x,\infty) = 0$. However, the compensation at $\mu = 0.5$ is not full because of

244   the nonlinearity of Γ in Eq. (5).

245

246   ***Diffusion-evaporation equation for DSD***

247   To formulate the diffusion-evaporation equation we use a simplified equation for droplet

248   evaporation (Pruppacher and Klett, 1997), in which the curvature term and the chemical

249   composition term are omitted

250     $$\frac{d\sigma}{dt} = \frac{2S}{F}$$ (12)

251   where $F = \dfrac{\rho_w L_w^2}{k_a R_v T^2} + \dfrac{\rho_w R_v T}{e_w(T)D} = const$ (Notations of other variables are presented in Appendix.)

252   The solution of Eq. (12) is

253     $$\sigma(t) = \frac{2}{F}\int_0^t S(t')dt' + \sigma_0$$ (13)

254   Eq. (13) means that in the course of evaporation, distribution $g(\sigma)$ shifts to the left without

255   changing its shape. The diffusion-evaporation equation for function $g(x,t,\sigma)$ can be written

256   in the form

257

258     $$\frac{\partial g}{\partial t} = K \frac{\partial^2 g}{\partial x^2} + \frac{\partial}{\partial \sigma}\left(\frac{d\sigma}{dt} g\right)$$ (14)

259   Combining Eqs. (12) and (14) yields

260     $$\frac{\partial g(x,t,\sigma)}{\partial t} = K \frac{\partial^2 g(x,t,\sigma)}{\partial x^2} + \frac{2S}{F}\frac{\partial g(x,t,\sigma)}{\partial \sigma}$$ (15)

261

262   Eq. (15) is similar to the diffusion-evaporation equation for size distribution function used in

263   Pt 3. The first term on the right hand side of Eq. (15) describes the effect of turbulent

264   diffusion, while the second term describes the changes of size distribution due to droplet

265   evaporation. To close this equation, one can use Eq. (5) written as

266

267     $S(x,t) = \exp\left[\Gamma(x,t) - A_2 q_w(x,t)\right] - 1,$ (16)

268

269   and the equation for liquid water mixing ratio

270

271     $q_w(x,t) = \frac{4\pi\rho_w}{3\rho_a}\int_0^\infty \sigma^{3/2} g(x,t,\sigma) d\sigma$ (17)

272   The equation system (15-17) for distribution $g(x,t,\sigma)$ should be solved under the following

273   initial condition

274     $g(x,0,\sigma) = \begin{cases} g_1(\sigma) & \text{if} & 0 \le x < \mu L \\ 0 & \text{if} & \mu L \le x < L \end{cases}$ (18)

275   and using the Neumann boundary conditions

276

277 $$\frac{\partial g(0,t,\sigma)}{\partial x} = \frac{\partial g(L,t,\sigma)}{\partial x} = 0 \qquad (19)$$

278

279   These equations were solved numerically on a linear grid of droplet radii r_j being within

280 the range 0-50 μm, where $j = 1...50$ are the bin numbers. The number of grid points along the

281 x-axis was set equal to 81. In numerical calculations, the "evaporation term" in Eq. (15) was

282 approximated as

283 $$\frac{2S}{F}\frac{\partial g(x,t,\sigma)}{\partial \sigma} \approx \frac{g\left(x,t,\sigma + \frac{2S}{F}\Delta t\right) - g(x,t,\sigma)}{\Delta t}. \qquad (20)$$

284

285 A shift and subsequent remapping of DSD using the method proposed by Kovetz and Olund's

286 (1969) were implemented to solve Eq. (20) with the help of MATLAB solver PDEPE. After

287 calculation of $g(x,t,\sigma_j)$ function, DSD $f(x,t,r_j)$ was calculated using the relationship

288 $f(x,t,r_j) = 2r_j g(x,t,\sigma_j)$.

289

290 **3. Spatial-temporal variations of DSD and of DSD parameters**

291   Mixing may take a significant time. Cloud microphysical parameters measured in *in-situ*

292 observations correspond to different stages of this transient mixing process. During mixing,

293 DSDs and its parameters change substantially, which makes it reasonable to analyze these

294 time changes.

295   **Figure 3** shows time evolution of initially narrow DSD in the centers of the cloudy volume

296 and of the initially dry volume. The values of DSD in the initially cloudy volume decrease

297 while there are no significant changes in the DSD shape. At $\mu = 0.7$, the droplet radius

298 corresponding to the DSD maximum remains unchanged during mixing staying equal to 10

299 μm. At $\mu = 0.3$ the effect of droplet diffusion on DSD is stronger, and mixing leads not

300 only to a decrease in the DSD values, but also to a decrease in the peak droplet radius in the

301 cloudy volume. Both at $\mu = 0.3$ and $\mu = 0.7$, mixing leads to broadening of the initial DSD

302 due to the appearance of the tail of small droplets.

303  In the center of the initially dry volume, the rate of the DSD growth depends on the value

304 of the cloud fraction. At a low cloud fraction, DSD maximum remains substantially lower for

305 the most period of mixing than that in the cloudy volume. At the same time, the radius

306 corresponding to the DSD maximum increases reaching 80% of its maximum value already

307 within the first 5 s. This is due to the fast increase in the relative humidity during mixing, so

308 large droplets penetrating the initially dry volume do not decrease in size anyhow significantly

309 determining the values of modal, mean volume and effective radii.

310

311 **Figure 3 here**

312

313  At the initially wide DSD (**Figure 4**), the radii of the DSD maximum do not change. It

314 means that at the initial RH= 80%, mixing and evaporation leads to a fast saturation of the

315 initially dry volume, after which the peak radius remains unchanged.

316

317

318 **Figure 4 here**

319

320

321 It is interesting that at $\mu = 0.3$ in the initially dry volume, DSD reaches its maximum during

322 the transition period (Fig.4, at t=80s), and then decreases toward the equilibrium state. This

323 behavior is caused by the competition between the diffusion and droplet evaporation.

324  **Figure 5** shows spatial dependences of droplet concentration, LWC and the effective

325 radius within the mixing volume at different time instances at narrow initial DSD. At small

326   values of the cloud fraction, diffusion of water vapor and droplets, as well as droplet

327   evaporation lead to a fast decrease in droplet concentration and in LWC in the initially cloud

328   volume. The effective radius in this volume decreases by about 12% in the course of mixing.

329   It is natural that at large cloud fraction, droplet concentration and LWC in the initially cloudy

330   volume decrease slowly, while these quantities in the initially dry volume increase rapidly At

331   both small and large cloud fractions, the effective radius in the initially dry volume grows

332   rapidly during the mixing toward its values in the initially cloudy volumes, even if droplet

333   concentration and LWC remain much lower than in the cloud volume.

334

335   **Figure 5 here**

336

337   **Figure 6** shows the spatial dependences of droplet concentration, LWC and the effective

338   radius within the mixing volume at different time instances at wide initial DSD.

339

340

341   **Figure 6 here**

342

343

344   A specific feature of mixing at a wide DSD is the increase in the effective radius, so the ratio

345   $\dfrac{r_e}{r_{e0}}>1$. In the course of mixing, the effective radius maximum is reached in the initially dry

346   volumes. This result can be attributed to the fact that in this volume smaller droplets fully

347   evaporate, so the concentration of large droplets increases with respect to concentration of

348   smaller droplets (Fig. 4, right column). Scattering diagrams plotted using *in-situ* observations

349   often contain points or groups of points with $\dfrac{r_e}{r_{e0}}>1$ (e.g. , Burnet and Brenguier, 2007;

350   Krueger et al., 2006, Gerber et al., 2008). In these observations, the effective radius was

351   measured within the cloud volume with maximum LWC (i.e. less diluted). The result obtained

352   in the present study shows that the behavior of $\dfrac{r_e}{r_{e0}}$ with time in the course of mixing may

353   depend of the DSD shape in the initially cloud volume.

354   We see that the transition to the final equilibrium state within the volume with the spatial

355   scale of 40 m is about 5 min (Fig. 8), which is a comparatively long period of time compared

356   to the characteristic times of other microphysical processes, including droplet evaporation.

357   During this time the DSD changes substantially, especially at small cloud fraction. The

358   effective radius in the initially dry volume increases much faster than LWC. As a result,

359   effective radius in such volume rapidly reaches the values typical of cloudy air, while LWC

360   still remains substantially lower than in the cloudy volume. Despite some DSD broadening,

361   the final DSDs in the mixing volume resemble those in the initially cloud volumes. The main

362   effect of mixing is lowering the DSD values as the cloud fraction decreases.

363

364   **4.   Equilibrium state and mixing diagram**

365   Mixing considered in the present study always leads to the equilibrium state. As was

366   explained above, two equilibrium states are possible. The first one is characterized by the total

367   evaporation of cloud droplets $q_w(x,\infty)=0$, whereas the second one occurs if the air in the

368   mixing volume becomes saturated, i.e. when $S(x,\infty)=0$. At the given initial values of q_{w1} in

369   the cloud volume and of S_2 in the initially dry volume, there always exists the cloud fraction

370   μ_{cr} (Eq. 11) separating these two states.

371

372   **4.1. The process of achieving the equilibrium state**

373   **Figure 7** shows the dependences of the time required to reach the equilibrium on the cloud

374   fraction, at different initial relative humidity values in the dry volume and two initial DSDs

375   (the parameters are presented in Tab.1). The characteristic time is defined here as the time

376   from the beginning of mixing to the time instance when inequality $\delta = \dfrac{\bar{N}(t) - \bar{N}(\infty)}{\bar{N}(0) - \bar{N}(\infty)} < 0.01$

377   becomes valid. The mean droplet concentration is calculated by averaging along x-axes

378   ($\bar{N}(t) = \dfrac{1}{L}\int\limits_0^L N(x,t)dx$). In case of a total evaporation, $\bar{N}(\infty) = 0$.

379

380   **Figure 7 here**

381

382   Each curve in Fig. 7 consists of two branches. The left branches correspond to the total

383   evaporation regime, while the right branches correspond to the partial evaporation at

384   equilibrium. The maximum time corresponds to the situation when the available amount of

385   liquid water is approximately equal to the saturation deficit. A similar result was obtained in

386   Pt1 and Pt2 for homogeneous mixing. The maximum values of the characteristic time are

387   about 4 min for a mixing volume of 40 m in length. The right branches show that the

388   characteristic time decreases with increasing cloud fraction. Despite some differences in the

389   curve slopes, the characteristic times for wide and narrow DSD are quite similar.

390   **Figure 8** shows dependences of normalized cube of the effective radius on the cloud

391   fraction at different time instances for two values of x: $x = 0$ (solid lines) corresponds to the

392   initially cloudy volume, and $x = L$ (dashed line) corresponds to the initially dry volume. The

393   figure is plotted for the narrow DSD for two values of RH_2: 60% and 95%. Despite the fact

394   that the diffusion-evaporation equation allows simulating using any initial RH, we do not

395   consider in our examples the cases of very low RH of dry volume. It is because at very low

396   RH, say, RH=20% , the cloud fraction should exceed 0.8 to prevent total droplet evaporation

397   in the equilibrium state (at LWC=1 g/kg). We believe that turbulence above the stratocumulus

398   cloud top is very weak and entrainment is slow, so cloud fraction should be large in this case.

399   At the lateral edges of warm Cu a shell of humid air arises around cloud, so RH of the

400   entrained air should be high enough (e.g. Gerber et al., 2008).

401

402

403

404   **Figure 8 here**

405

406   The curve plotted for the time instance of 300 s corresponds to the equilibrium state (hereafter

407   the equilibrium curve). The curves above the equilibrium curve correspond to the initially

408   cloudy volume, and the curves below the equilibrium curve correspond to the initially dry

409   volume. One can see how curves of both types approach the same final state. During the

410   mixing the curves move over the $\left(\dfrac{r_e}{r_{e0}}\right)^3 - \mu$ plane toward the equilibrium curve. As a result,

411   the curves plotted in Fig.8, corresponding to different time instances of the mixing, together

412   cover the entire area of the panels.

413   During this movement the distance from the curves to the horizontal line $\left(\dfrac{r_e}{r_{e0}}\right)^3 = 1$ changes,

414   and the curves slopes increase. In our case of $L = 40\,\text{m}$, the mixing remains inhomogeneous

415   the during entire mixing process, so the change in the distance from the curves to the

416   horizontal line $\left(\dfrac{r_e}{r_{e0}}\right)^3 = 1$ characterizes the temporal changes over the mixing process, but not

417   a change in mixing type.

418   It is noteworthy in this relation that scattering diagrams plotted using *in-situ* observations

419   reflect mixing between different multiple volumes at different stages of the mixing process.

420   Accordingly, points in the scattering diagrams can be far from the equilibrium location. Fig. 8

421   indicates, therefore, that scattering diagrams show snapshots of transient mixing process when

422   the distance from points in the diagrams to line $\left(\dfrac{r_e}{r_{e0}}\right)^3 = 1$ characterize the stage of the

423   mixing process, but not the mixing type.

424   The dependences of normalized cube of the effective radius on the cloud fraction at different

425   time instances at wide DSD also indicate approaching to the equilibrium curve, while all the

426   curves correspond to $\left(\dfrac{r_e}{r_{e0}}\right)^3 > 1$ (not shown). In most studies normalized cube of mean

427   volume radius is used for plotting the mixing diagrams. Note, however, that since effective

428   radius in a wide range of conditions is only by 10% larger than the mean volume radius, the

429   utilization of effective radius does not affect the results. Moreover, satellites measure

430   specifically effective radius. Accordingly, some authors (e.g. Freud et al., 2011) use effective

431   radius for plotting the mixing diagrams.

432

433   **4.2. Mixing diagrams**

434   Using the diffusion-evaporation equations (15-17) we calculated the equilibrium DSD for

435   different initial relative humidity values and different cloud fractions. Each calculation was

436   performed for both narrow and wide initial DSD (parameters shown in Tab.1). These

437   equilibrium DSD were used to calculate mixing diagrams showing dependences of normalized

438   cube of the effective radius on the cloud fraction.

439   The corresponding mixing diagrams for   homogeneous mixing case were also calculated

440   for comparison. To this effect, the supersaturation and DSD in both the cloud and the dry

441   volumes were aligned, taking into account the cloud fraction value μ. The alignment led to

442   the following initial values of supersaturation and DSD within the mixing volume:

443

444    $S_0 = (1-\mu)S_2;\quad g_0(\sigma) = \mu g_1(\sigma)$ (21)

445

446   Upon the alignment, time evolution values of DSD under homogeneous evaporation in an

447   adiabatic immovable parcel were calculated until the equilibrium state was reached. These

448   equilibrium DSD were used to calculate mixing diagrams for homogeneous mixing. To do

449   this, we used the parcel model proposed by Korolev (1995) that describes evaporation by

450   means of equations with temperature-dependent parameters. **Figure 9** shows the mixing

451   diagrams plotted for initial narrow and wide DSD cases.

452

453   **Figure 9 here**

454

455

456   While all the curves in the mixing diagram for narrow DSD are below the straight line

457    $\left(\dfrac{r_e}{r_{e0}}\right)^3 = 1$, the curves for wide DSD are above this line. The explanation of this effect is given

458   in Section 3 (Fig. 6). The curves plotted for homogeneous and inhomogeneous mixing

459   demonstrate an important feature. Namely, at given values of RH and q_{w1} in the initially dry

460   volume, the values μ_{cr} of the cloud fraction at which all the droplets evaporate are

461   approximately the same for any type of mixing. This condition is the consequence of the mass

462   conservation law determined by Eq. (11) and does not depend of the initial DSD shape. In

463   standard mixing diagrams (e.g. Lehmann et al., 2009; Gerber et al., 2008; Freud et al., 2011),

464   the horizontal straight line $\left(\dfrac{r_e}{r_{e0}}\right)^3 = 1$ is typically plotted for the entire range of the cloud

465   fraction [0...1], while the curves corresponding to homogeneous mixing are plotted for

466   different RH within the range $[\mu_{cr}(RH_2)...1]$. As a result, the high difference between

467   extremely inhomogeneous and homogeneous mixing types is clearly seen at low RH and at

468   small cloud fractions. The condition that μ_{cr} is the same for different mixing types indicates

469   that the mixing diagrams may look nearly similar for $\mu > \mu_{cr}$. It means that the range of the

470   cloud fractions required for comparison of diagrams aimed at determination of a mixing type

471   shortens as RH_2 values in the surrounding air decrease.

472   The comparison of the left and the right panels in Fig. 9 shows that the differences

473   between the diagrams for homogeneous and inhomogeneous mixing types are more

474   pronounced for initially narrow DSD. The maximum difference should take place for

475   monodisperse DSD considered in in Pt1, Pt2 and Pt3. Within the range of $\mu > \mu_{cr}$, the

476   distance between the curves corresponding to different mixing regimes is small even for

477   narrow DSD and low RH_2. The lower difference is related to the fact that at high RH_2 the

478   curves in the mixing diagrams are close to the horizontal straight line in both regimes, while at

479   low RH_2, μ_{cr} is small and both curves should drop to zero in the vicinity of $\mu = \mu_{cr}$.

480   As regards the wide DSD case, the difference between the curves corresponding to

481   different mixing type is negligible (Fig. 9, right)

482

483   **4.3. Effect of the relative humidity**

484   In measurements carried out at cloud boundaries and in cloud simulations, the cloud

485   fraction is not known, therefore it is widely accepted to use normalized droplet concentration

486   instead of the cloud fraction (Burnet and Brenguier, 2007; Gerber et al., 2008: Lehmann et al.,

487   2009). Droplet concentration is normalized by the maximum value along the airplane traverse.

488   The difference between the cloud fraction and normalized droplet concentration is obvious:

489   the cloud fraction is a parameter given as the initial condition. At the same time, normalized

490   droplet concentration changes with time and space due to complete evaporation of some

491   droplet fraction. **Figure 10** shows dependencies of normalized droplet concentration on the

492   cloud fraction at the equilibrium final state of mixing. One can see a substantial deviation

493   from 1:1 linear dependence, especially at low RH. As we know, droplet concentration

494   decreases in the course of both homogeneous and inhomogeneous mixing if the initial DSD

495   are polydisperse. The fraction of totally evaporating droplets increases with decreasing RH_2.

496 As expected, droplet concentration in homogeneous mixing is higher than that in

497 inhomogeneous mixing. The difference between droplet concentrations at wide DSD is lower

498 than at narrow DSD.

499

500 **Fig. 10 here**

501

502 **Figure 11** shows the dependencies $\left(\dfrac{r_e}{r_{e0}}\right)^3$ on normalized droplet concentration for narrow

503 and wide DSD in inhomogeneous mixing. The normalization by droplet concentration in the

504 initially cloud volume at $t = 0$ was used. Taking into account the dependences of normalized

505 droplet concentration on the cloud fraction μ (Fig. 10), one can get the curves shown in Fig.

506 11 which actually coincide at different RH_2. The lack of the sensitivity to RH_2 can be

507 attributed to the fact that a decrease in RH leads to a decrease in normalized droplet

508 concentration, so the curves corresponding to low RH in Fig. 9 shift to the left when the

509 normalized droplet concentration is used instead of μ. The shape of the dependences in Fig

510 11 (right) is explained by an increase in the effective radius with decreasing droplet

511 concentration.

512

513 **Fig 11 here**

514

515 Thus, the mixing diagrams plotted in the plane $\left(\dfrac{r_e}{r_{e0}}\right)^3$ vs normalized droplet

516 concentration do not depend on the relative humidity of the surrounding dry air. This result

517 indicates an additional difficulty in distinguishing between mixing types based on scattering

518 diagrams plotted using *in-situ* data in these axes. The concentration of observed points in

519 these scattering diagrams close to the line $\left(\dfrac{r_e}{r_{e0}}\right)^3 = 1$ is often interpreted as an indication of

520 homogeneous mixing, but at high RH in the surrounding air (Gerber et al., 2008; Lehmann et

521 al., 2009). High values of RH in the penetrating air volumes are usually explained by

522 formation of a layer of most air around the cloud boundary (Gerber et al., 2008, Knight and

523 Miller, 1998).

524   The reference values of droplet concentration and the effective radius used for

525 normalization in the present study are taken as the initial values in the cloud volume before it

526 mixes with the neighbouring dry volume. In real *in-situ* measurements the reference values of

527 these quantities are typically chosen in a less diluted cloud volume along the airplane traverse.

528 This reference volume may be quite remote from the particular mixing volume. It can lead to

529 a shift of the mixing diagram with respect to the $\left(\dfrac{r_e}{r_{e0}}\right)^3 = 1$ line, as well as to a large variation

530 in mixing diagram shapes, unrelated, however, to the mixing type (e.g., Lehmann et al.,

531 2009).

532

533   **5.**   **Discussion and conclusion**

534   This study extends the analysis of mixing performed in Pt3 where the diffusion-

535 evaporation equation served as the basis, the initial DSD were assumed monodisperse and

536 the cloud fraction was chosen as $\mu = 1/2$. In the present study, the analysis focuses on the

537 temporal and spatial evolution of initially polidisperse DSD and investigates mixing diagrams

538 obtained for narrow and wide initial DSD within a wide range of the cloud fraction values (

539 0.1 - 0.95). It is shown that results of mixing and the structure of mixing diagrams depend on

540 the initial DSD shape. This finding indicates that mixing is a multi-parametrical problem that

541 cannot be determined by a single parameter (e.g. the Damkölher number as often assumed) or

542 even by two parameters (the Damkölher number and the potential evaporation parameters as

543 assumed in Pt3). The temporal changes of DSD and their moments during mixing are

544 calculated. Although DSD broaden, they tend to remain similar to the original DSD. The main

545 changes come from the cloud air dilution by the dry air, which leads to a decrease in droplet

546 concentration for all droplet sizes. The changes of DSD and its shape are minimum in the

547 initially cloud volumes, especially at significant cloud fractions. The droplet radii

548 corresponding to the DSD peak do not change anyhow significantly. In the initially dry

549 volumes, mixing leads to a rapid increase in RH. Consequently, large droplets penetrating

550 these volumes do not change their sizes significantly. As a result, the effective radius in these

551 volumes rapidly increases and reaches the values typical of cloud volumes, while LWC

552 remains lower than in the cloud volume for most of the mixing time. At narrow DSD, the

553 effective radius remains smaller than that in the initially cloud volume. At wide DSD, the

554 effective radius may become larger than that in the initial DSD. This increase in the effective

555 radius is attributed to the fact that evaporation of smaller droplets leads to the increase in the

556 fraction of larger droplets in the DSD. Note that the DSD broadening caused by mixing is the

557 consequence of the utilization of polydisperse DSDs. In classical theory that assumes

558 monodisperse DSDs no broadening takes place. This problem is analyzed in detail in Pt 3.

559 Note that in real clouds DSD there are many mechanism leading to DSDs broadening (e.g.

560 Pinsky and Khain 2002).

561   Dependences of normalized cube of the effective radius on the cloud fraction $\left(r_e / r_{e0} \right)^3$ as

562 a function of μ at different time instances form the set of curves filling the entire

563 $\left(r_e / r_{e0} \right)^3 - \mu$ plane. Therefore, both the slope and the distance of these curves in respect to

564 the horizontal line $\left(r_e / r_{e0} \right)^3 = 1$ change with time. It means that this distance characterizes

565 the temporal changes in the course of mixing, but not the mixing type (which remains

566 inhomogeneous during the entire mixing time). The mixing process is comparatively long

567 (several minutes), so the final equilibrium stage is hardly achievable in real clouds.

568   It is highly significant that the critical values of the cloud fraction μ_{cr} corresponding to

569   total droplet evaporation are the same for any mixing type. It means that the curves in a

570   mixing diagram corresponding to homogeneous and inhomogeneous mixing types should be

571   compared only within the range of $\mu > \mu_{cr}$. The range width of $\mu > \mu_{cr}$ decreases with

572   decreasing relative humidity in the initially dry volume. Taking into account significant

573   scattering of observed points, this condition greatly hampers the problem of how to

574   distinguish between mixing types,

575   Another important result of the study is that mixing diagrams for homogeneous and

576   inhomogeneous mixing plotted for polydisperse DSD do not differ much. The largest

577   difference takes place for initially narrow DSD (the maximum difference should take place for

578   initial monodisperse DSD), but even in this case the difference is not large enough to reliably

579   distinguish mixing type due to the significant scatter of observed data. At wide DSD, this

580   difference becomes negligibly small.

581   The cloud fraction μ is a predefined parameter and is not determined from observations.

582   Consequently, in the analysis of *in-situ* measurements the normalized droplet concentration is

583   typically used instead of the cloud fraction. However, there is a significant difference between

584   the cloud fraction prescribed a priori and the normalized droplet concentration that changes

585   due to total evaporation of some fraction of droplets. We have shown that utilization of

586   normalized droplet concentration in mixing diagrams is not equivalent to utilization of the

587   cloud fraction. The important conclusion is that when mixing diagrams are plotted using the

588   normalized concentration, the dependence on the RH disappears. This conclusion is valid even

589   when the RH in the initially dry volume is as low as 60%. This conclusion clearly contradicts

590   the wide-spread assumption that mixing types can be easily distinguished in mixing diagrams

591   in case of low relative humidity of the surrounding air.

592   To sum up, our general conclusion is that the simplifications underlying the classical

593   concept of mixing are too crude, making it impossible to use mixing diagrams for

594 comprehensive analysis of mixing and especially for determination of the mixing type. At the

595 same time, mixing diagrams may contain useful information on DSD width.

596

597   *Acknowledgements*

598   This research was supported by the Israel Science Foundation (grants 1393/14, 2027/17)

599 and the Office of Science (BER) of the US Department of Energy (Award DE-SC0006788,

600 DE-FOA-0001638). Codes of the diffusional-evaporation model are available upon request.

601   .

602

603

604

605   **Appendix. List of symbols**

Symbol	Description	Units
A_2	$\dfrac{1}{q_v}+\dfrac{L_w^2}{c_p R_v T^2}$, coefficient	-
a_n	Fourier series coeficients	-
C	Richardson's law constant	-
c_p	specific heat capacity of moist air at constant pressure	J kg^{-1}K^{-1}
D	coefficient of water vapor diffusion in air	m^2 s^{-1}
Da	*Damkölher* number	-
e	water vapor pressure	N m^{-2}
e_w	saturation vapor pressure above flat surface of water	N m^{-2}
F	$\left(\dfrac{\rho_w L_w^2}{k_a R_v T^2}+\dfrac{\rho_w R_v T}{e_w(T)D}\right)$, coefficient	m^{-2} s
$f(r)$	droplet size distribution	m^{-4}
$g(r)$	droplet size distribution	m^{-5}

$g_0(\sigma)$	initial distribution of square radius in homogeneous mixing	m^{-5}
$g_1(\sigma)$	initial distribution of square radius	m^{-5}
k_a	coefficient of air heat conductivity	$J\ m^{-1}s^{-1}K^{-1}$
K	turbulent diffusion coefficient	m^2s^{-1}
L	characteristic spatial scale of mixing	m
L_w	latent heat for liquid water	$J\ kg^{-1}$
N	droplet concentration	m^{-3}
N_0	Parameter of Gamma distribution	m^{-3}
$\bar{N}$	mean droplet concentration	m^{-3}
N_1	initial droplet concentration in cloud volume	m^{-3}
p	pressure of moist air	$N\ m^{-2}$
q_v	water vapor mixing ratio (mass of water vapor per 1 kg of dry air)	-
q_w	liquid water mixing ratio (mass of liquid water per 1 kg of dry air)	-
q_{w1}	liquid water mixing ratio in cloud volume	-
R	$\dfrac{S_2}{A_2 q_{w1}}$, non-dimensional parameter	-
R_a	specific gas constant of moist air	$J\ kg^{-1}K^{-1}$
R_v	specific gas constant of water vapour	$J\ kg^{-1}K^{-1}$
r	droplet radius	m
r_1	initial droplet radius	m
r_e	effective radius	m
r_{e0}	initial effective radius	m
S	$e/e_w - 1$, supersaturation over water	-

S_2	initial supersaturation in the dry volume	-
S_0	initial supersaturation in homogeneous mixing	-
T	temperature	K
t	time	s
x	distance	m
α	parameter of Gamma distribution	-
β	parameter of Gamma distribution	m^{-1}
Δt	time step	s
μ	cloud fraction	-
μ_{cr}	critical cloud fraction	-
ε	turbulent dissipation rate	$m^2 s^{-3}$
$\Gamma(x,t)$	conservative function	-
ρ_a	air density	$kg\ m^{-3}$
ρ_w	liquid water density	$kg\ m^{-3}$
σ	square of droplet radius	m^2

606

607

608

609

610

611

612

613

614

615

References

Andrejczuk, M., W. W. Grabowski, S. P. Malinowski, and P. K. Smolarkiewicz, 2009: Numerical simulation of cloud–clear air interfacial mixing: Homogeneous versus inhomogeneous mixing, *J. Atmos. Sci.*, **66(8),** 2493-2500, doi:10.1175/2009JAS2956.

Bera, S., T. V. Prabha, and W. W. Grabowski, 2016a: Observations of monsoon convective cloud microphysics over India and role of entrainment-mixing, *J. Geophys. Res. Atmos.*, **121**, 9767–9788, doi:10.1002/2016JD025133.

Bera, S., G. Pandithurai and T. V. Prabha, 2016b: Entrainment and droplet spectral characteristics in convective clouds during transition to monsoon. *Atmos. Sci. Let.* **17**, 286–293.

Boffetta, G. and Sokolov, I. M., 2002: Relative dispersion in fully developed turbulence: The Richardson's law and intermittency correction, *Phys. Rev. Lett.*, **88**, 094501, doi:10.1103/PhysRevLett.88.094501.

Burnet, F., and J.-L Brenguier, 2007: Observational study of the entrainment-mixing process in warm convective cloud, *J. Atmos. Sci.*, **64**, 1995–2011.

Devenish B. J., P. Bartello, J-L. Brenguier, L.R. Collins, W.W. Grabowski, R.H.A. Ijzermans, S.P. Malinovski, M.W. Reeks, J.C. Vassilicos, L-P. Wang, and Z. Warhaft, 2012: Droplet growth in warm turbulent clouds. *Q. J. Roy. Meteorol. Soc.*, **138**, 1401-1429.

Freud, E., D. Rosenfeld, and J. R. Kulkarni, 2011: Resolving both entrainment mixing and number of activated CCN in deep convective clouds, *Atmos. Chem. Phys.*, **11**, 12,887–12,900, doi:10.5194/acp-11-12887-2011.

Gerber H, Frick G, Jensen J.B, and Hudson J.G., 2008: Entrainment, mixing, and microphysics in trade-wind cumulus. *J. Meteorol. Soc. Jpn.,* **86A**. 87-106.

Khain, A. P., M. Ovchinnikov, M. Pinsky, A. Pokrovsky, and H. Krugliak, 2000: Notes on the state-of-the-art numerical modeling of cloud microphysics. *Atmos. Res.*, **55**, 159-224.

Khain A., Thara V. Prabha, N. Benmoshe, G. Pandithurai, M. Ovchinnikov, 2013: The mechanism of first raindrops formation in deep convective clouds. *J. Geoph. Res. Atmospheres*, **118**, 9123–9140.

Khain A., M. Pinsky and L. Magaritz-Ronen, 2017: Physical interpretation of mixing diagrams. *J. Geophys. Res.* (in revision)

Knight C. A. and L. J. Miller, 1998: Early radar echoes from small, warm cumulus: Bragg and hydrometeor scattering. *J. Atmos. Sci.,* **55**, 2974-2992.

Korolev, A.V., 1995: The influence of suresaturation fluctuations on droplet size spectra formation. *J. Atmos. Sci.*, **52**, 3620-3634.

Korolev A., and I. Mazin, 2003: Supersaturation of water vapor in clouds, *J. Atmos. Sci.*, **60**, 2957-2974.

Korolev, A., Khain, A., Pinsky, M., and French, J., 2016: Theoretical study of mixing in liquid clouds – Part 1: Classical concept, *Atmos. Chem. Phys.*, **16**, 9235–9254.

Kovetz, A., and B. Olund, 1969: The effect of coalescence and condensation on rain formation in a cloud of finite vertical extent. *J. Atmos. Sci.,* **26,** 1060–1065.

Krueger, S. K., Lehr, P. J., & Su, C. W., 2006: How entrainment and mixing scenarios affect droplet spectra in cumulus clouds. In *12th Conference on Cloud Physics, and 12th Conference on Atmospheric Radiation,* Madison, WI.

Kumar, B., J. Schumacher, and R. A. Shaw, 2014: Lagrangian mixing dynamics at the cloudy–clear air interface. *J. Atmos. Sci.*, **71**, 2564-2579.

Kumar, B., S. Bera, T. V. Prabha, and W. W. Grabowski, 2017: Cloud-edge mixing: Direct numerical simulation and observations in Indian Monsoon clouds, *J. Adv. Model. Earth Syst.*, **9**, doi:10.1002/2016MS000731.

Lehmann, K.., H. Siebert, and R. A. Shaw, 2009: Homogeneous and inhomogeneous mixing in cumulus clouds: Dependence on local turbulence structure. *J. Atmos. Sci.*, **66**, 3641-3659.

665   Magaritz-Ronen. L., M. Pinsky, and A. Khain, 2016: Drizzle formation in stratocumulus

666   clouds: effects of turbulent mixing. *Atmos. Chem. Phys*., **16**, 1849–1862, doi:10.5194/acp-16-

667   1849.

668   Monin, A.S. and Yaglom, A.M. 1975: "Statistical Fluid Mechanics: Mechanics of

669   Turbulence", vol. **2**, MIT Press.

670   Pinsky, M., Khain, A. P., 2002: Effects of in-cloud nucleation and turbulence on droplet

671   spectrum formation in cumulus clouds. *Quart. J. Roy. Met. Soc*., **128**, 1-33.

672   Pinsky, M., Khain, A., Korolev, A., and Magaritz-Ronen, L., 2016a: Theoretical investigation

673   of mixing in warm clouds – Part 2: Homogeneous mixing, *Atmos. Chem. Phys*., **16**, 9255–9272.

674   Pinsky, M., Khain, A., and Korolev, A., 2016b: Theoretical analysis of mixing in liquid

675   clouds – Part 3: Inhomogeneous mixing, *Atmos. Chem. Phys*., **16**, 9273–9297.

676   Polyanin A. D. and V. F. Zaitsev, 2004: Handbook of nonlinear partial differential equations.

677   Chapman & Hall/CRC, 809 pp.

678   Prabha T., Khain, A. P., B. N. Goswami, G. Pandithurai, R. S. Maheshkumar, and J. R.

679   Kulkarni, 2011: Microphysics of pre-monsoon and monsoon clouds as seen from in-situ

680   measurements during CAIPEEX. *J. Atmos. Sci.,* **68**, 1882-1901.

681   Pruppacher, H.R., Klett, J.D., 1997. Microphysics of Clouds and Precipitation. 2nd edn.

682   Oxford Press, 914 p.

683   Segal, Y., Khain, A. P., and M. Pinsky, 2003: Theromodynamic factors influencing the

684   bimodal spectra formation in cumulus clouds. *Atmos. Res.* **66**, 43-64.

685   Yang F., R. Shaw, and H. Xue, 2016: Conditions for super-adiabatic droplet growth after

686   entrainment   mixing   *Atmos.   Chem.   Phys.,*   **16**,   9421–9433,   www.atmos-chem-

687   phys.net/16/9421/2016/ doi:10.5194/acp-16-9421-2016.

688   Yum, S. S., J. Wang, Y. Liu, G. Senum, S. Springston, R. McGraw, and J. M. Yeom, 2015:

689   Cloud microphysical relationships and their implication on entrainment and mixing mechanism

690   for the stratocumulus clouds measured during the VOCALS project, *J. Geophys. Res.*, **120(10)**,

691   5047-5069, 10.1002/2014JD022802.

692

693

694

695

696

697

698

699

700

701

702

703

704

705

706

707

708

709

710

711

712

713

714

715

716

717 **Tab.1** Parameters of the initial Gamma distributions

DSD	N_0, cm^3	α	β, μm	Modal radius, μm	LWC, g/m^3
Narrow	264.2	101.0	0.1	10.0	1.178
Wide	71.0	4.3	3.1	10.0	1.178

718

719

720

721

722

723

724

725

726

727

728

729

730

731

732

733

734

735

736

737

738

739

740   Figures

741

742

743

744

745

746

747

748

749

750

751

752

753

754
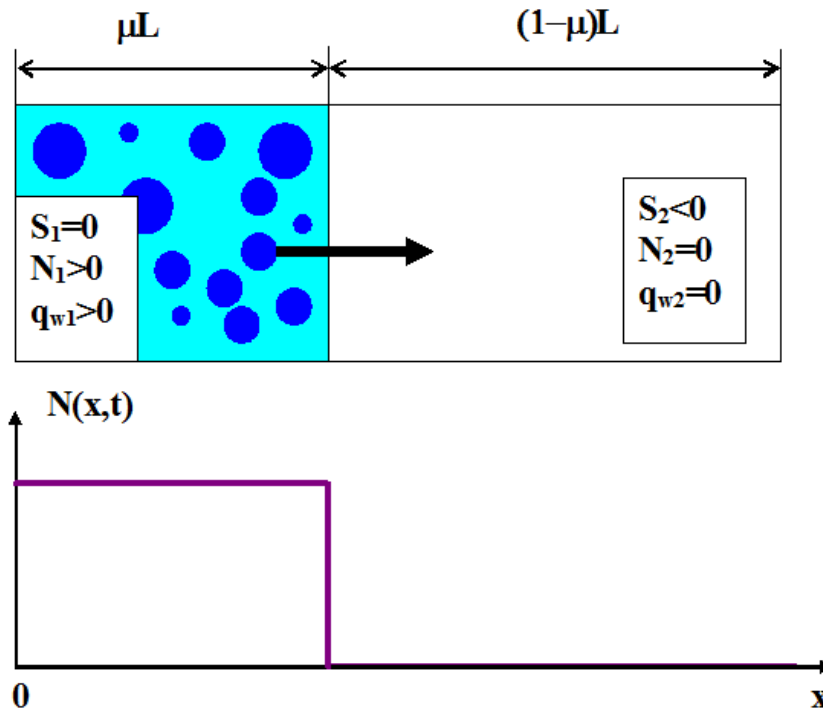
755   **Fig.1.** The initial state at $t = 0$. The left volume is a saturated cloudy volume; the right

756   volume is an under-saturated dry air volume.

757

758

759

760

761

762

763

764

765

766

767
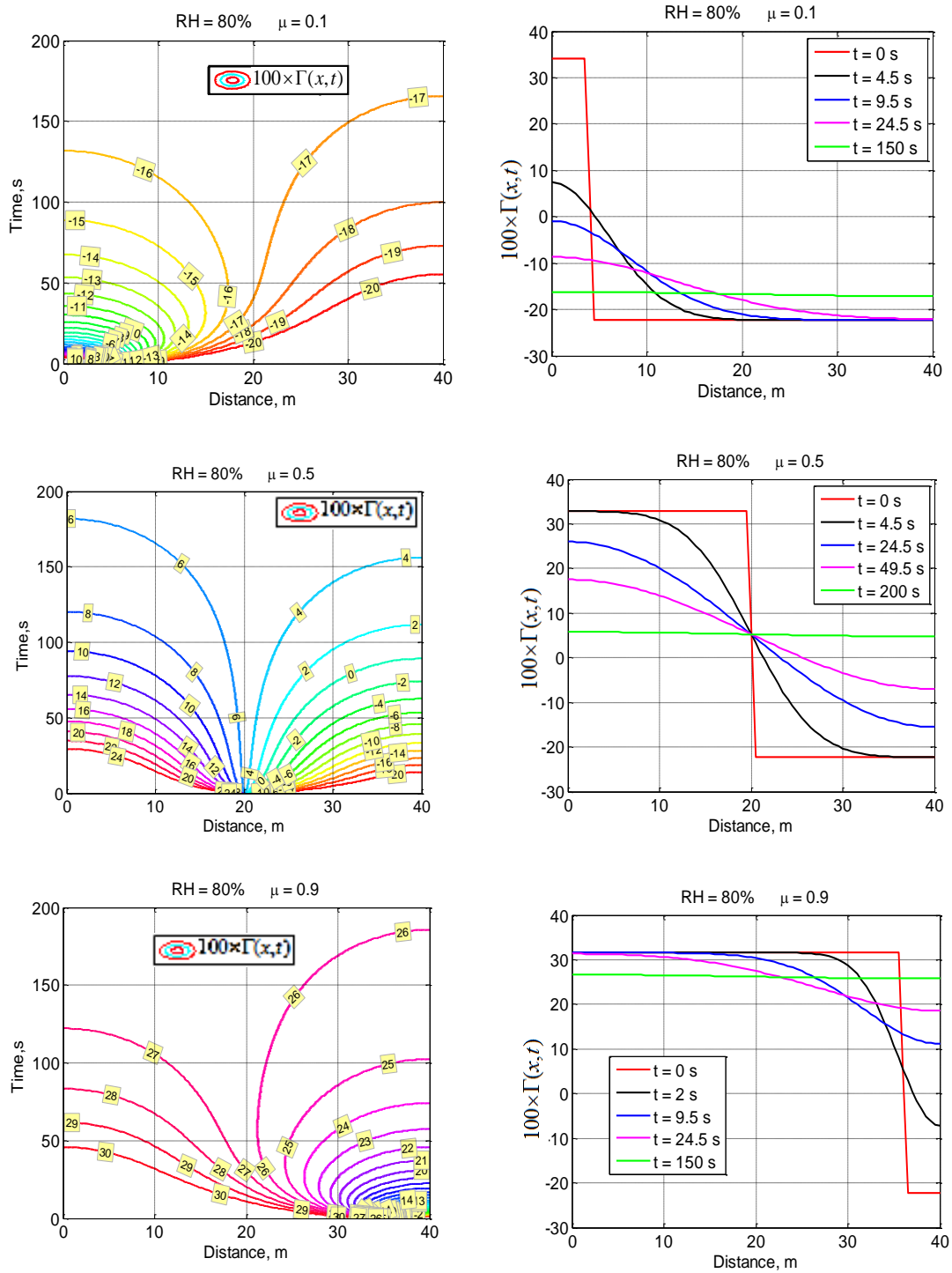
788   **Fig. 2.** Spatial-temporal variations of conservative function $100 \times \Gamma(x,t)$ for different cloud

789   fractions μ and initial $RH_2 = 80$ % .

790

791

792

793

794

795

796

797

798

799

800

801

802

803

804

805

806

807

808
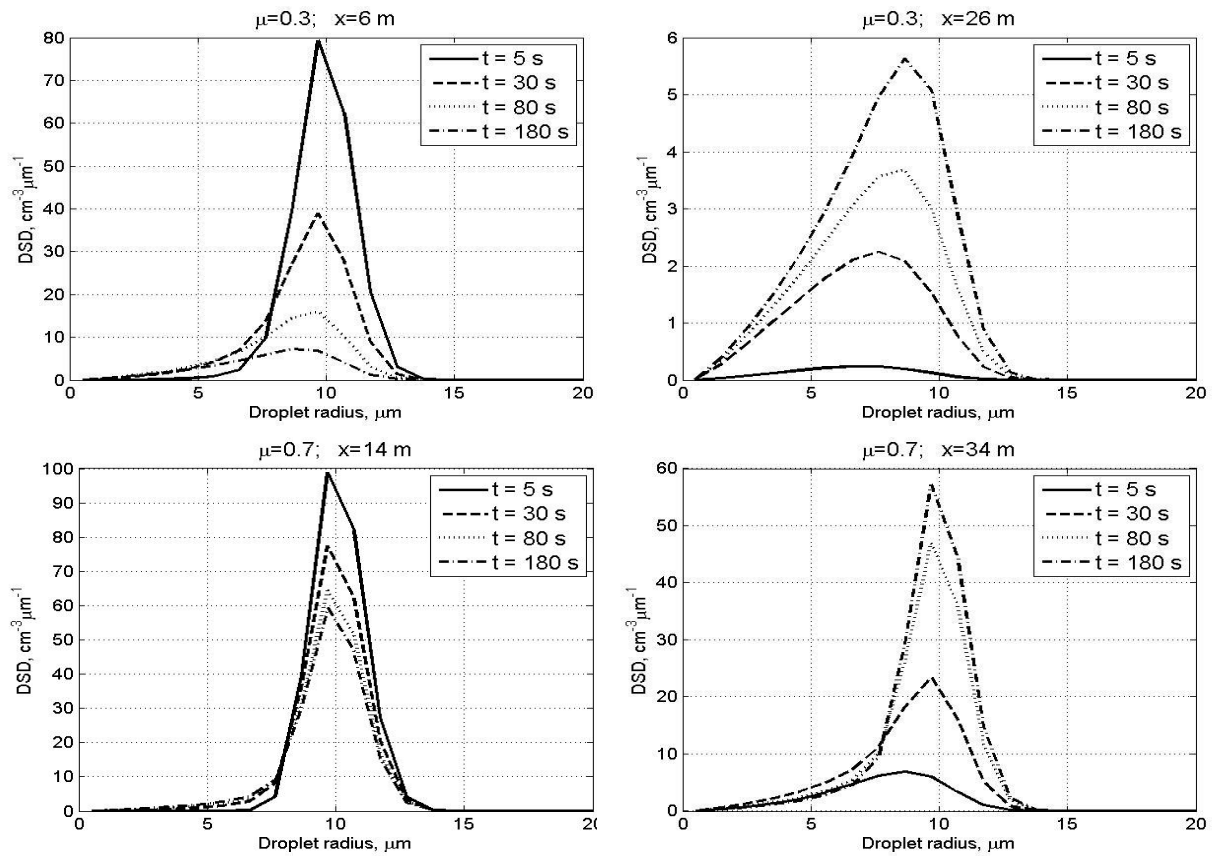
Fig. 3. Time evolution of DSD in the centers of the initially cloudy volume (left) and of the

initially dry air volume (right) at initially narrow DSD. The initial mixing parameters are

$RH_2 = 80\,\%$, $T = 10^{\circ}C$, $p = 828.8$ mb and $L = 40$ m.

812

813

814

815

816

817

818

819

820

821

822

823

824

825

826

827

828

829

830

831

832

833

834

835

836
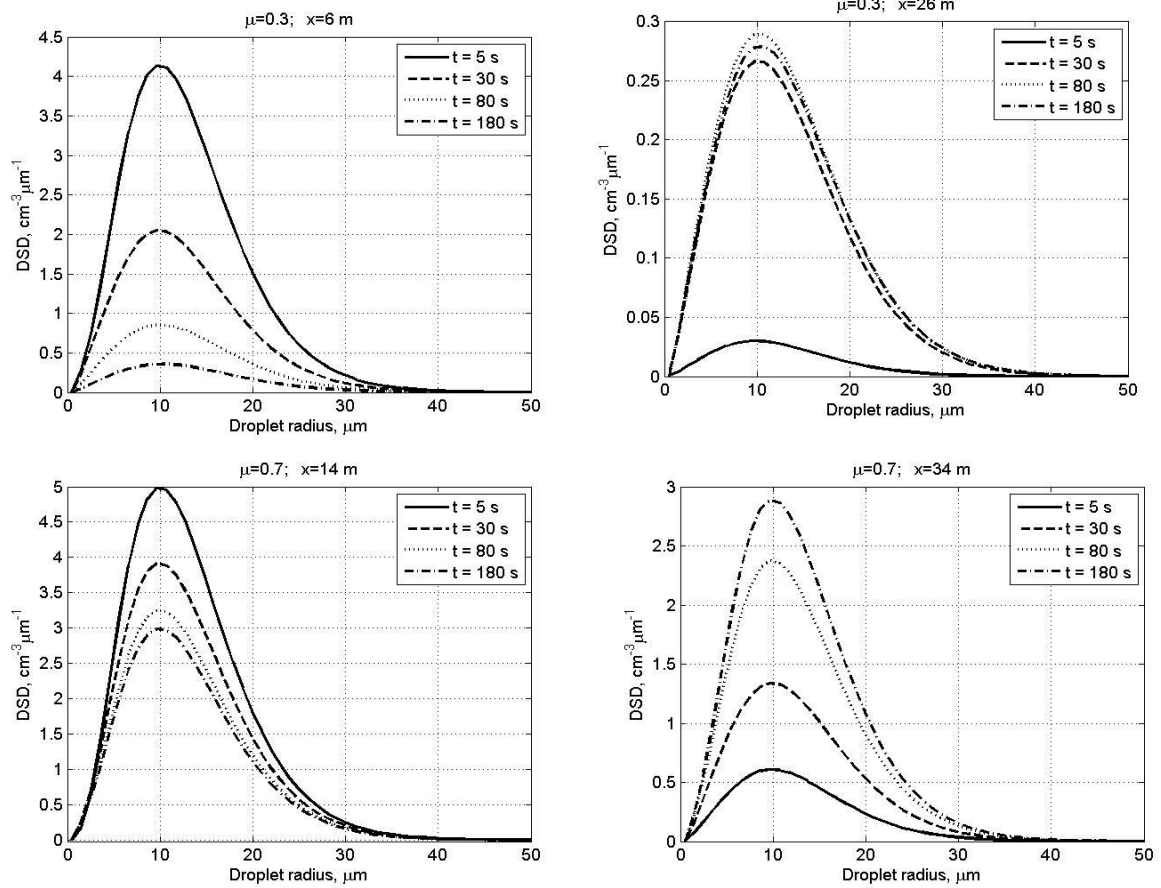
837 **Fig. 4.** The same as in Fig. 3, but for the initially wide DSD.

838

839

840

841

842

843

844
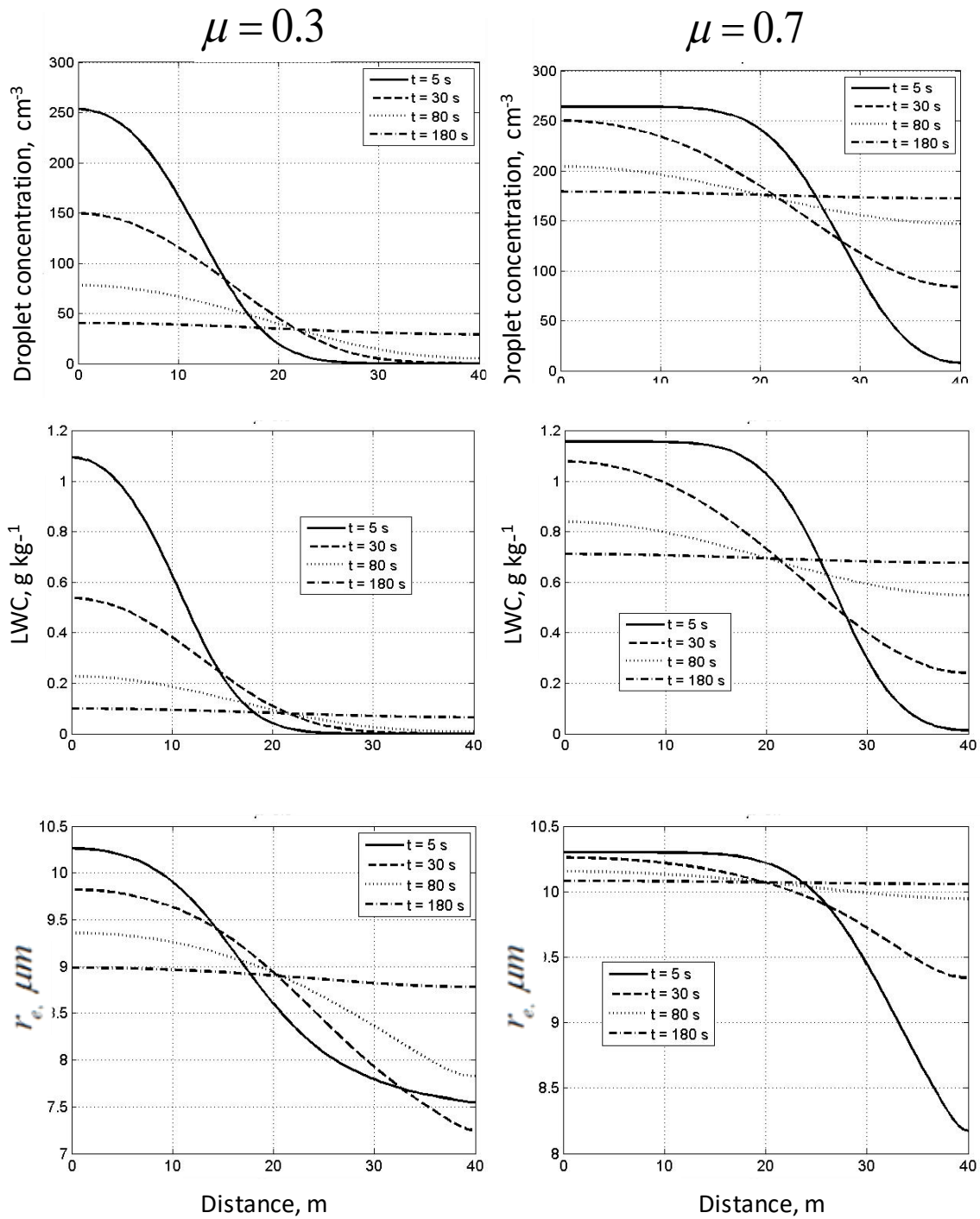
845 **Fig. 5.** Spatial dependences of droplet concentration, LWC and the effective radius within the

846 mixing volume at different time instances at narrow initial DSD. The initial mixing

847 parameters are $RH_2 = 80\,\%$, $T = 10^{\circ}C$, $p = 828.8$ mb and $L = 40$ m.

848
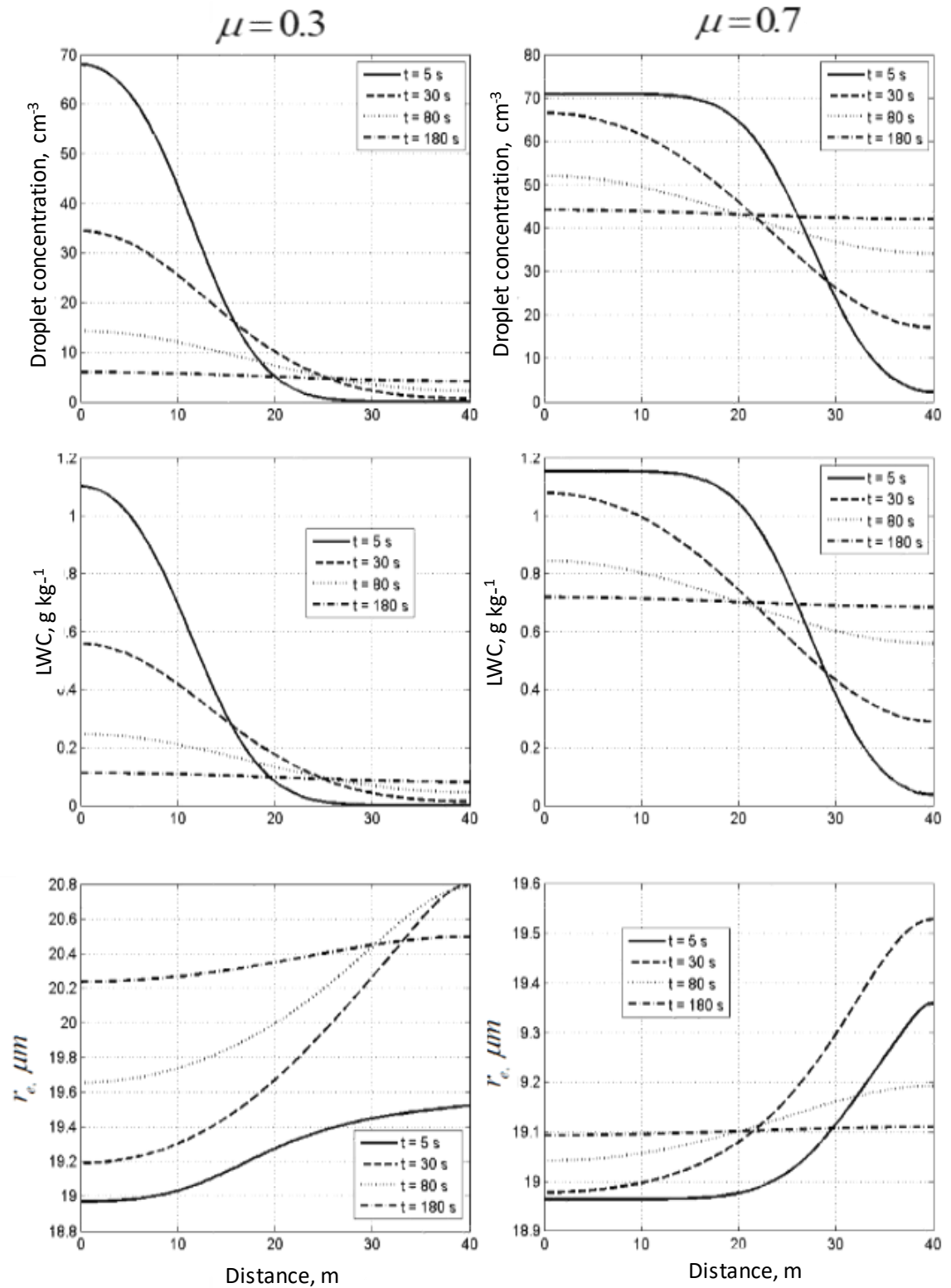
Fig. 6. The same as in Fig. 5, but for wide DSD

854

855

856

857

858

859

860

861

862

863

864

865

866

867

868

869

870
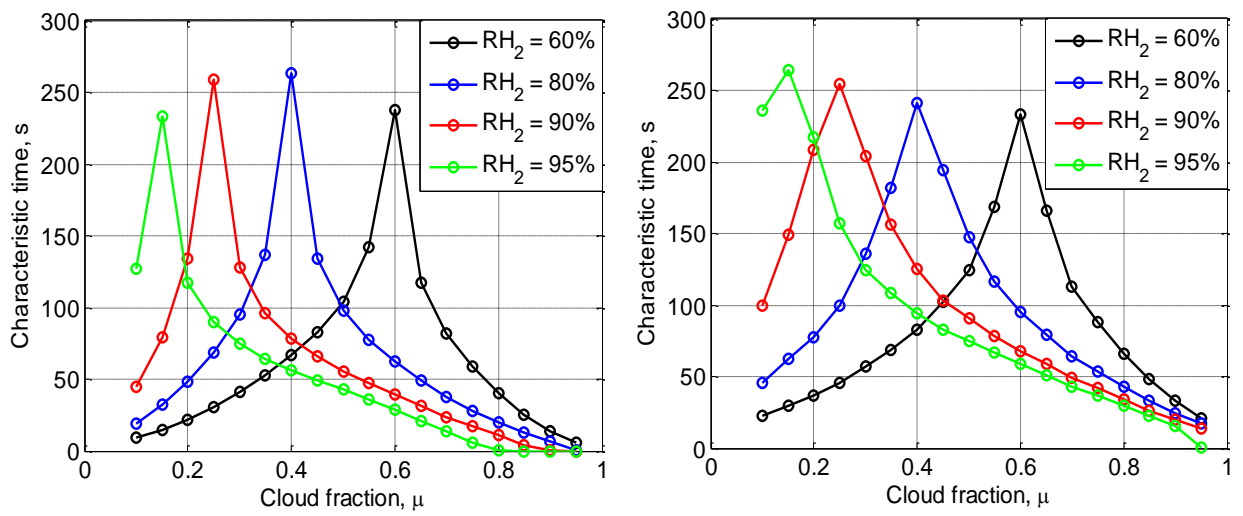
Fig. 7. Time required to reach the equilibrium state vs. the cloud fraction at different

initial RH for the initially narrow DSD (left) and the initially wide DSD (right). Parameters of

DSD are given in Tab. 1. The initial mixing parameters are $T = 10^{\circ}C$, $p = 828.8$ mb and

$L = 40$ m.

875

876

877

878

879

880

881

882

883

884

885

886

887

888

889

890

891

892

893

894

895

896
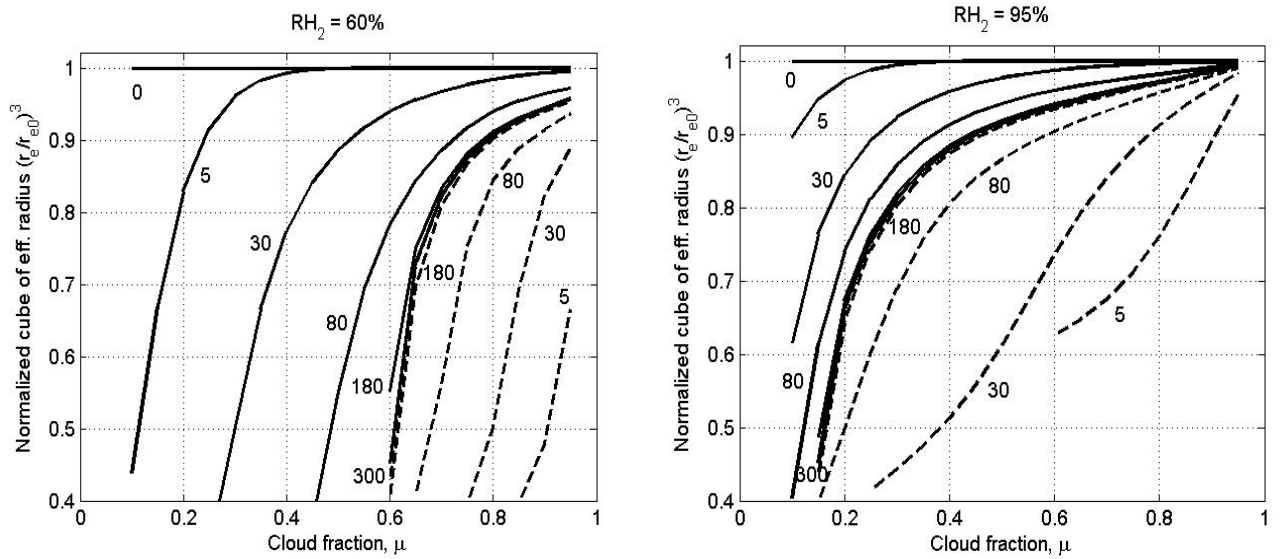
897   **Fig. 8.** Dependences of normalized cube of the effective radius on the cloud fraction at

898   different time instances for $x = 0$ (solid lines) corresponding to the initially cloud volume,

899   and $x = L$ (dash line) corresponding to the initially dry volume. The time instances in seconds

900   are marked by numbers. The figure is plotted for the narrow initial DSD for two values of

901   RH_2: 60% (left panel) and 95% (right panel). Parameters of DSD are given in Tab. 1. The

902   initial mixing parameters are $T = 10^{\circ}C$, $p = 828.8$ mb and $L = 40$ m. Calculations performed

903   within the range of $0.1 < \mu < 0.95$.

904

905

906

907

908

909

910

911

912

913

914

915

916

917

918

919

920

921
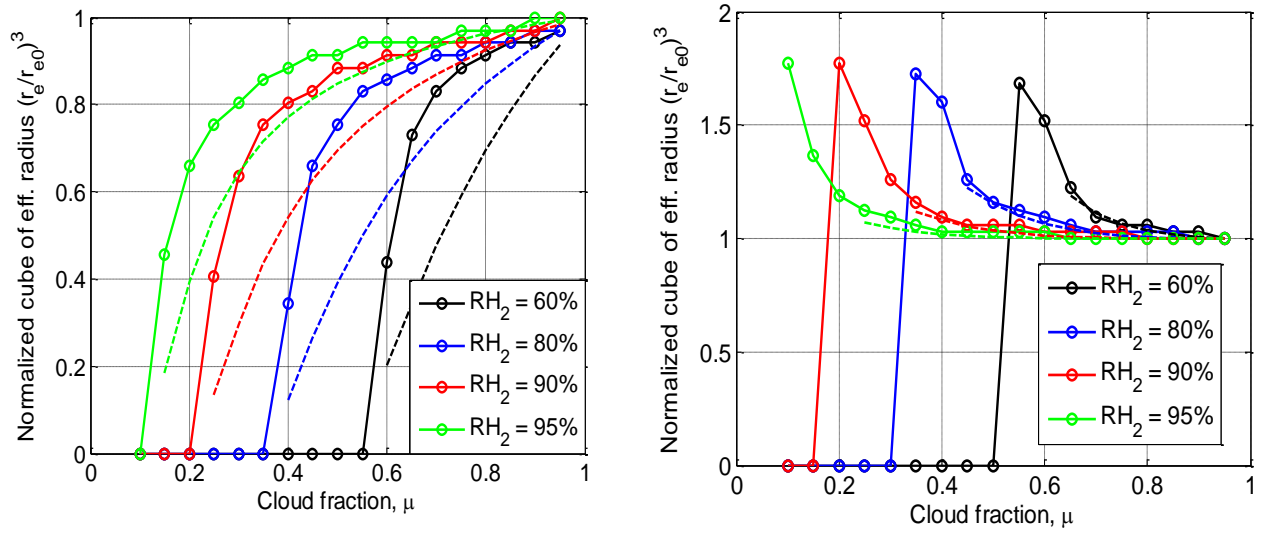
Fig. 9. Mixing diagrams. Normalized cube of the effective radius vs. the cloud fraction for initial narrow DSD (left) and initial wide DSD (right). The dependencies correspond to the equilibrium state Parameters of initial DSD are presented in Tab. 1. Solid and dashed lines show the mixing diagrams for inhomogeneous and homogeneous mixing, respectively. The initial mixing parameters are $T = 10^{\circ}C$, $p = 828.8$ mb and $L = 40$ m.

927

928

929

930

931

932

933

934

935

936

937

938

939

940

941

942

943

944

945

946

947

948

949
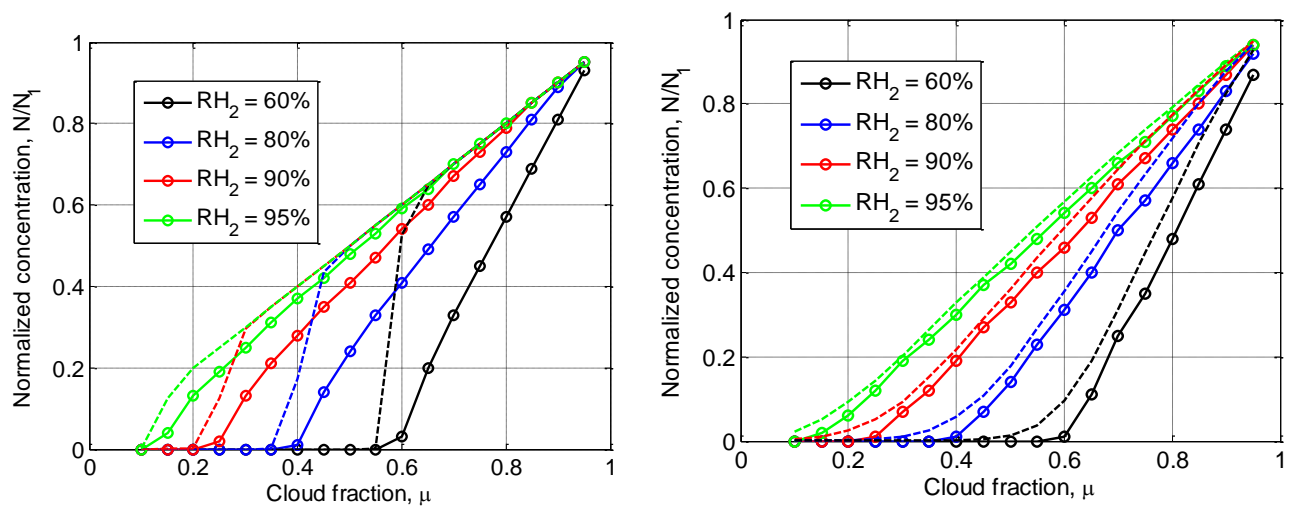
950   **Fig. 10.** Final normalized droplet concentration vs. cloud fraction for initially narrow DSD

951   (left) and initially wide DSD (right). Parameters of initial DSD are shown in Tab. 1. Dashed

952   line shows the results of equivalent homogeneous mixing. The initial mixing parameters are

953    $T = 10^{\circ}C$, $p = 828.8$ mb and $L = 40$ m.

954

955

956

957

958

959

960

961

962

963

964

965

966

967
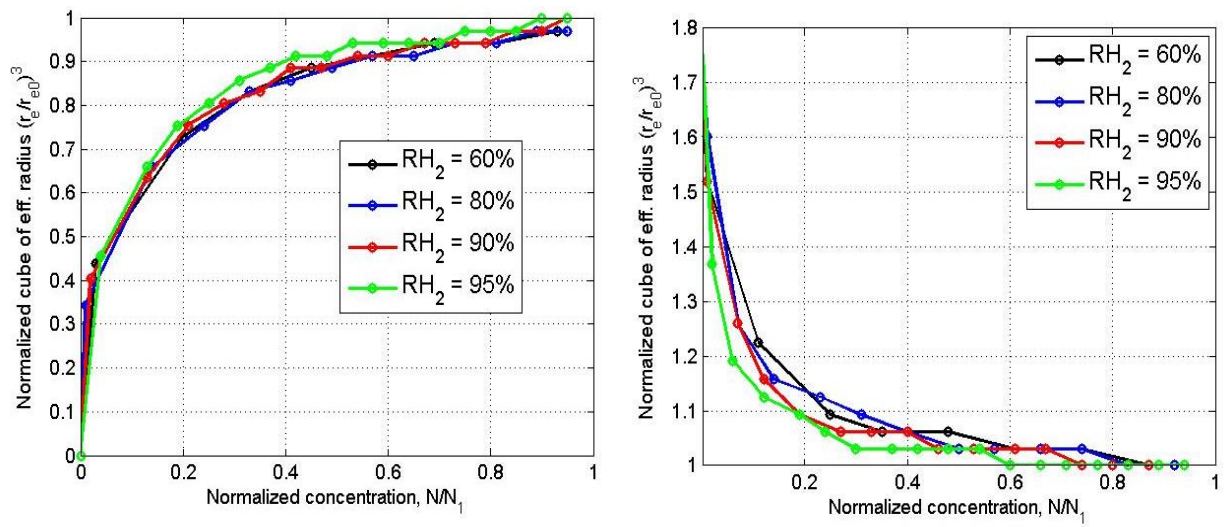
Fig. 11. Dependencies of normalized cube of the effective radius on normalized droplet concentration for different initial relative humidity values. Left panel: narrow initial DSD. Right panel: wide initial DSD. The initial mixing parameters are $T = 10^{\circ}C$, $p = 828.8$ mb and $L = 40$ m.

972

973

974